

OPEN GEOMECHANICS

X-ray tomography analysis of particle morphology influence on granular deformation processes

Gustavo Pinzon^{id a, b}, **Edward Andò**^{id c},
Alessandro Tengattini^{id b, d, e} & **Gioacchino Viggiani**^{id b}

^a European Synchrotron Radiation Facility, Grenoble, France

^b Laboratoire 3SR, Université Grenoble Alpes, Grenoble, France

^c École Polytechnique Fédérale de Lausanne, EPFL Center for Imaging, Lausanne, Switzerland

^d Institut Laue-Langevin, Grenoble, France

^e Institut Universitaire de France, IUF, France.

Published

25th March 2025

<https://doi.org/10.5802/ogeo.21>

Edited by

Benjy Marks

The University of Sydney
Australia

Reviewed by

Anonymous Reviewer

Dong Wang

Yale

United States of America

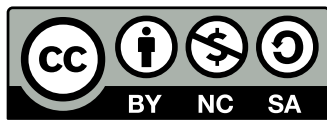
Correspondence

Gustavo Pinzon

European Synchrotron Radiation Facility,
Grenoble, France

gustavo.pinzon-forero@esrf.fr

Laboratoire 3SR, Université Grenoble
Alpes, Grenoble, France



This article is licensed under the Creative Commons Attribution
NonCommercial ShareAlike 4.0 License.



Open Geomechanics is member of the
Centre Mersenne for Open Scientific Publishing

Abstract. The interaction between particles in granular materials is largely determined by their shape and interparticle friction. Thus, understanding their combined effects is essential for modelling the mechanical behaviour at the bulk scale. Previous studies have focused on the link between the morphology of the particles and the bulk response of the specimen. The emergence of non destructive full-field techniques, such as x-ray tomography, present a novel opportunity for the detailed quantification of key particle-scale phenomena. This study investigates the impact of inter-particle friction and particle shape on the deformation processes of granular materials through *in-operando* x-ray tomography. Monodisperse specimens, comprising ellipsoidal particles with a given aspect ratio and interparticle friction coefficients, are here tested under triaxial compression conditions. Three values of aspect ratio and two friction coefficients are explored, yielding in total six specimens. Over 30 scans per test are acquired, every 0.5% of axial shortening. Each of the more than 20000 individual particles are identified and tracked throughout a test. Strain localisation dominates post-peak stress ratio, forming compressive and dilative zones within the shear band. The results show that higher aspect ratios lead to an increase of volumetric strain, while lower interparticle friction makes the response less dilative. The study of the interplay between particles interlocking and rotation, reveals that particles with a mild degree of anisometry and high friction yield the highest degree of bulk dilatancy, due to a balancing between the interlocking and rotation.

Keywords. Strain localisation, X-ray tomography, Particle kinematics, Granular materials

1. Introduction

Granular materials are composed of particles, whose morphology plays a crucial role on the way they interact with each other. Particle shape can be described at many different scales, from which, three are traditionally considered [Santamarina and Cho, 2004], each of them marked by a characteristic length. The first length scale is the one of the particle itself, *i.e.*, its overall proportions. Two classification methodologies are conventionally employed. One approach describes particles based on the relation between an orthogonal set of axes, *e.g.*, Zingg [1935] proposes a common classification among different shapes (*e.g.*, Oblates, Prolates, Bladed, and Equant). Alternatively, the resemblance of the particle shape to a sphere can be used (*e.g.*, by Wadell [1932]) as a metric, employing the concept of *true sphericity*, which is the ratio of the surface area of a sphere of equivalent volume to the considered particle with its actual surface.

A second scale can be identified where the features that are smaller than the particle diameter are considered. These features are linked to the surface roundness, which can also be used to classify particles. Particle *roundness* can be for example measured by assessing the average curvature of edges and corners relative to the overall particle curvature [Krumbein, 1941]. Finally, a third scale examines particle surface topography, considering features of several orders of magnitude smaller than the particle diameter [Katainen et al., 2006]. Despite the clear multi-scale nature of particle shape, it is usually presented using opposing scenarios from each scale, such as sphericity as opposed to ellipticity, roundness as opposed to angularity, and smoothness as opposed to roughness [Santamarina and Cho, 2004].

An early example of the study of the grain-scale origins of the response of granular media is Miura et al. [1998], which studied correlations between the macroscopic mechanical properties of natural sands with the morphology of constituent particles. For example it has been observed that higher void ratios can be achieved when non-spherical or angular particles are used, as a result of the additional edges and corners that restrain particle mobility (*e.g.*, Abbireddy and Clayton [2015], Rousé et al. [2008]). Correspondingly, angular particles yield an overall higher peak stress ratio and critical state friction angle, which is correlated to the formation of inherently anisotropic assemblies (*e.g.*, Miura et al. [1998], Santamarina and Cho [2004]). Additionally, angularity increases the degree of interlocking between the particles, *i.e.*, the motion of a given particle is constrained by its neighbours (*e.g.*, Xiao et al. [2019]).

The advent of non-invasive techniques, such as x-ray tomography, allowed the quantification of particle-based quantities and their spatial distribution, non destructively, for the first time [Andò and Viggiani, 2018, Hall et al., 2010, Oda et al., 2004]. These direct measurements have shown that the degree of anisometry of particles, *i.e.*, the degree of deviation from a sphere of an ellipsoid, affects their rotation [Kong and Fonseca, 2019], which in turn impacts the strain localisation patterns [Andò et al., 2013]. These particle-based measurements enable the identification of

the deformation mechanism which control the bulk response of the specimen.

Complementary to physical experiments, numerical simulations have been extensively used, since the morphology of the particles can be easily simulated and parameterized. Simple geometries, such as ellipses [Rothenburg and Bathurst, 1992], overlapping disks [Saint-Cyr et al., 2011], polygons [Azéma et al., 2007] and polyhedral [Azéma et al., 2013] are commonly used to represent particle shape. Contact laws have been modified to include rolling resistance at the contacts to account for particle angularity [Estrada et al., 2011, Rorato et al., 2021], attempting to emulate the behaviour of complex geometries while maintaining the computational simplicity of disks/spheres.

Numerical simulations allow an easy access to the study of the initial packing. For example it has been observed that a higher degree of connectivity is produced with higher anisometry of the particles [Azéma et al., 2013, Rothenburg and Bathurst, 1992, Saint-Cyr et al., 2011]. They have also been employed to connect the macroscopic shear strength [Azéma et al., 2012, 2007, Pena et al., 2007], bulk volumetric strain [Azéma and Radjaï, 2010, Mirghasemi et al., 2002, Zhou et al., 2013] and peak dilatancy at peak stress [Azéma and Radjaï, 2010, Rothenburg and Bathurst, 1992] to the angularity (or, more specifically, the rolling resistance) of the particles.

Beside these geometrical considerations, another first-order parameter governing the response of the particle assemblies is interparticle friction. Few experimental studies focus on this, and have mainly studied surface roughness as a surrogate of particle friction, highlighting a positive correlation with the macroscopic response in terms of peak stress ratio, peak dilatancy [Alshibli and Alsaleh, 2004], as well as the overall morphology of the strain localisation region [Alsaleh et al., 2006]. Cavarretta et al. [2011] designed a novel inter-particle friction apparatus, allowing the measurement of the friction coefficient between two particles under controlled conditions. However, the intrinsic variability of natural materials hinders the possibility to univocally isolate friction in physical experiments. Numerical simulations are more commonly adopted to tackle this question, because of the straightforward manner in which the value of friction can be altered through contact laws. Simulation results show a positive correlation between interparticle friction and shear strength, maximum volumetric strain, and peak dilatancy angle [Antony and Kruyt, 2009, Barreto and O'Sullivan, 2012, Binaree et al., 2020, Casas et al., 2022, Taboada et al., 2005].

Previous studies, both experimental and numerical, address independently the effects of particle shape and interparticle friction. Yet, to the best of the authors' knowledge, there is a gap in the literature regarding the interplay between these two very important features. This is particularly evident for physical experiments, where the systematic isolation of the effects of particle shape and interparticle friction proves exceptionally challenging.

This work aims to shed light onto the interplay between particle shape and interparticle friction, with a specific focus on their influence on the deformation processes of

granular materials. Injection moulded plastic ellipsoids are here chosen as surrogate materials so as to finely control their morphological characteristics, and talc powder is used to control their inter-particle friction. To isolate and magnify the impact these parameters, a monodisperse distribution of particles is deliberately used. These granular assemblies are tested under triaxial compression conditions while acquiring multiple x-ray tomographies for each test, in order to gather data on the evolving granular microstructure, as revealed by image analysis procedures. All the data used and presented in this work are available in an open access repository [Pinzón et al., 2023].

2. Methods

2.1. Experimental setup

Oblate ellipsoidal particles made of polyoxymethylene (POM) are employed here to study the effects of particle shape and friction. To guarantee controlled and repeatable conditions, an injection-moulding process is used to manufacture them, resulting in thousands of particles with the same morphological characteristics. The ratio between the long and short axis of the oblate ellipsoids (*i.e.*, the aspect ratio), is used as a measure of particle shape. Three sets of particles are manufactured, each with a specific aspect ratio. The first set, referred to as *flat* particles, has full axes of 2.2 mm × 3.4 mm × 3.4 mm, resulting in an aspect ratio of 1.55. The second set, referred to as *medium* particles, has full axes of 3.0 mm × 3.4 mm × 3.4 mm, resulting in an aspect ratio of 1.13. The third set, referred to as *rounded* particles, has full axes of 3.23 mm × 3.4 mm × 3.4 mm, resulting in an aspect ratio of 1.05.

Based on the work of Senetakis and Coop [2014], an inter-particle shearing device is built to characterise the inter-particle friction angle by measuring the resulting forces at the contact point using a 6-axis forcemeter, similar to the one used in Shahin and Hurley [2022]. The friction angle is taken as the maximum value registered as the pair of particles are sheared. Following the work of Oda et al. [1982], talc powder is used to modify the surface characteristics, reducing inter-particle friction angle. This allows the creation of two distinctive friction scenarios: rough and smooth, characterised by an average inter-particle friction angle of 9° and 5°, respectively.

By combining the three aspect ratios and the two inter-particle friction values, a total of six testing conditions are obtained. Cylindrical specimens 70 mm in diameter and 140 mm in height are prepared using a dry pluviation method, resulting in more than 20000 monodisperse particles in each specimen. Based on the work of Yuan et al. [2021], the minimum and maximum void ratios of each shape-friction pair can be computed analytically since both indices are functions of the excluded volume due to the shape of the particles. As shown in Table 1, the initial relative density ranges from 64 % to 76 %, suggesting a limited variability of the initial void ratio.

Table 1. Initial parameters of the tested specimens: Aspect ratio (AR), Interparticle friction angle (μ), Relative density (D_r), and particle anisotropy (ζ_P).

Specimen	AR	μ	D_r [%]	ζ_P
Flat-Rough	1.54	$9.06^\circ \pm 2.26^\circ$	75.33	0.162
Flat-Smooth	1.54	$5.25^\circ \pm 1.30^\circ$	76.97	0.077
Medium-Rough	1.13	$8.81^\circ \pm 2.13^\circ$	66.40	0.140
Medium-Smooth	1.13	$4.98^\circ \pm 0.92^\circ$	67.98	0.129
Rounded-Rough	1.05	$9.16^\circ \pm 2.14^\circ$	64.76	0.044
Rounded-Smooth	1.05	$5.55^\circ \pm 1.32^\circ$	68.32	0.084

Triaxial compression tests are performed imposing a confining stress of 50 kPa, which is attained by applying a controlled vacuum inside the specimen. A non-conventional triaxial compression setup is used, which includes a sliding base on one of the ends as show in Fig. 1. This promotes the failure of the specimen to occur along a unique shear band, concentrating higher local values of deviatoric strain. The experiments are performed *in-operando* inside the x-ray tomography cabin at Laboratoire 3SR (Grenoble, France) at a compression rate of $4 \mu\text{m s}^{-1}$, performing the scans each 0.5 % of axial shortening. The tests are stopped when the edge of the sliding base contacts the internal wall of the cell. The x-ray tomography scans are performed using a voxel size of $100 \mu\text{m}/\text{vox}$. Further details on image acquisition and the experimental setups can be found in Pinzón [2023].

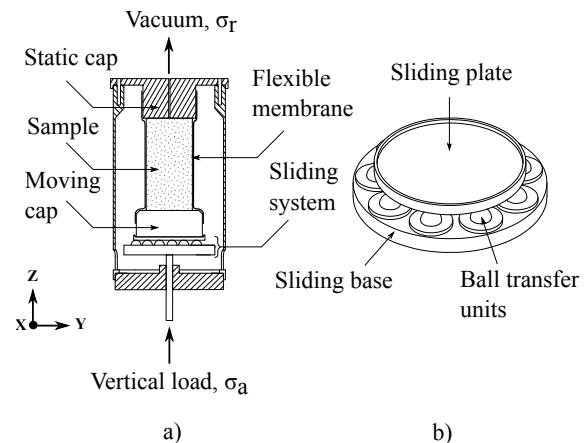


Figure 1. Diagram of the triaxial compression cell used in this study: a) General overview, and b) detailed view of the sliding base

2.2. Image analysis

At each scan, a 3D greyscale volume of $1456 \times 1456 \times 1840$ pixels is obtained using a filtered back-projection algorithm. This set of greyscale volumes represents the raw data from which all other measurements of this study are derived. The open-source software *spam* [Stamati et al., 2020] is used to obtain the measurements detailed hereafter.

A greyvalue thresholding algorithm, followed by a watershed algorithm are used to identify and label each particle from the initial greyscale volume. The quality of this initial

segmentation is thoroughly inspected, and manual corrections are performed until a “golden-standard” initial segmentation is obtained, *i.e.*, a labelled volume which reflects as closely as possible the real morphology of the grains. This time-consuming procedure is only performed for the first scan of each experiment.

A novel approach is implemented to track 100% of the particles throughout each experiment, marking the first time that all individual grains are successfully followed at every strain increment. This is achieved using the iterative algorithm developed by Tudisco et al. [2017] in the “Discrete DVC” mode of Hall et al. [2010]. In essence, the tracking procedure requires to determine the linear transformation function that delineates the deformation of each grain between a reference state and a deformed state. Details about the underlying implementation of the tracking algorithm can be found in Andò et al. [2019]. Once all particles are tracked successfully, the measured transformation of each particle is applied to the labelled image, so as to obtain a new labelled volume for the second scan. While this resulting labelled volume would be sufficient to directly assess the spatial attributes of particles (*e.g.*, position and orientation), it is here instead used as the basis for a further watershed algorithm, which helps to better resolve the edges and interactions between them: in short the deformed voxelised labels are used as markers for watershed segmentation of the binarised deformed image. The deformed labelled volume thus obtained is employed for the tracking of particles in the subsequent strain increment. This iterative process is repeated increment-by-increment, yielding a distinct labelled volume for each scan, while preserving the labels of the particles. Ensuring accurate particle tracking between successive scans is crucial to prevent the propagation of any labelling errors. To achieve this, the tracking procedure for a given strain increment is iteratively performed until *all* particles within the specimen are accurately tracked.

These results are used to obtain the evolution of the macroscopic deformation as well as the 3D strain fields for each increment of each specimen. The macroscopic axial shortening (ϵ_a) and volumetric strain (ϵ_V) are measured directly from each scan as proposed in Pinzón [2023]. The axial shortening is defined as $\epsilon_a = (L_0 - L_i)/L_0$, where L_0 and L_i are the height of the overall sample, obtained through binary filling the segmented images at the initial and deformed state, respectively. Similarly, the macroscopic volumetric strain is measured as $\epsilon_V = (V_0 - V_i)/V_0$, where V_0 and V_i are the volumes of the binary-filled images at the initial and deformed state, respectively. Positive values are assigned to volume reduction (contraction), following the usual soil mechanics convention.

The particle tracking results are used to compute the strain fields inside the specimens. Each particle displacement vector is projected onto a regularly spaced 3D grid, following the 2D approach of Desrues and Viggiani [2004]. The spacing of the elements in this grid needs to be selected with care, as it has significant effects on the resulting strain fields. In order to set it in an objective way, a Delaunay tessellation using the particle centres as nodes is first performed, resulting in a space-filling tetrahedral mesh linking

particle centres – which *can* be used to compute strains in granular materials as detailed in Bagi [1996] and Zhang and Regueiro [2015]. However this is not done here because the resulting strains are found to be noisy given that the gradient is measured only on four points. Instead, we use the average volume of the tetrahedral elements to set the size of the 3D grid: points are spaced so that their enclosed cubic volume is the same as the average tetrahedron. This results in a grid spacing of 40 pixels, to be compared to the longer axis of the particles measuring around 34 pixels.

To compute strains from interpolated particle displacements, the grid is now considered as a regular mesh containing Q8 cubic elements, and a transformation gradient tensor is computed at its centre employing the displacement vectors of the corresponding nodes. The volumetric (ϵ_V) and deviatoric strains (ϵ_q) for each cubical element can then be easily computed, using the right stretch tensor (U) obtained through a polar decomposition of the transformation gradient tensor. Specifically, the volumetric strain is computed as the first invariant of the strain tensor as $J - 1$, while the deviatoric strain is computed as the second invariant of the strain tensor as $\|1/J^{1/3} \cdot U\|$, where J is the determinant of the transformation gradient tensor.

Beside the displacement of each particle, obtained directly from the particle tracking, the rotation of particles can also be computed by measuring the rotation of their orientation vector. This is represented using a vector-angle system, following Euler’s rotation theorem, *i.e.*, an arbitrary rotation of a body (ω) can be described to a single rotation of magnitude $\|\omega\|$ along a given axis (e_ω), so that $\omega = \|\omega\|e_\omega$. Given the oblate shape of the particles, the orientation vector is taken as the direction of the minor axis. Given two orientation vectors of a particle at different instants of the test (v_1 and v_2), the magnitude of rotation is computed as $\|\omega\| = \cos^{-1}((v_1 \cdot v_2)/(\|v_1\|\|v_2\|))$; while the axis of rotation is defined as: $e_\omega = v_1 \otimes v_2$, where \otimes is the cross product. The error associated to the orientation measurement is related to the shape of the particle, and it is measured at $\pm 1^\circ$ for the rounded particles, $\pm 0.5^\circ$ for the medium particles, and $\pm 0.1^\circ$ for the flat particles. It is important to note that the rotation of the particles along their axis of symmetry is not resolved using the proposed approach. However, this along-axis rotation has only a second-order effect, primarily affecting energy dissipation at the contact level, as it does not influence the orientation of neighboring particles nor the local particle arrangement.

Finally, the degree of bulk anisotropy of particle orientation (ζ_P) can be computed using the particle orientation vectors, using the implementation detailed in Nadler et al. [2018]. In essence, the plausible range of this scalar anisotropy goes from the extreme case of $\zeta_P = 1$, where all the particles are perfectly aligned towards the same direction, to the perfectly isotropic distribution of $\zeta_P = 0$. The evolution of particle anisotropy and fabric, in general, falls outside the scope of this study and is addressed in an upcoming complementary article. However, noticeable differences in the initial values of ζ_P in Table 1 indicate significant variations in the internal arrangement of particles,

influenced by their shape and friction angle, even before the application of the external load.

3. Results

3.1. Macroscopic response

Figure 2 shows the evolution of the macroscopic response of the specimens, in terms of the evolution of the stress ratio (q/p) and of the volumetric strain (ε_v), as a function of the axial shortening of the specimens. The deviatoric stress q is defined as $\sigma_1 - \sigma_3$, while the mean stress p is defined as $(1/3)(\sigma_1 + 2\sigma_3)$, where σ_1 and σ_3 denote the major and minor principal stresses, respectively. The recurring drops in the stress ratio correspond to stress relaxation when the loading system is paused in order to perform the X-ray scans.

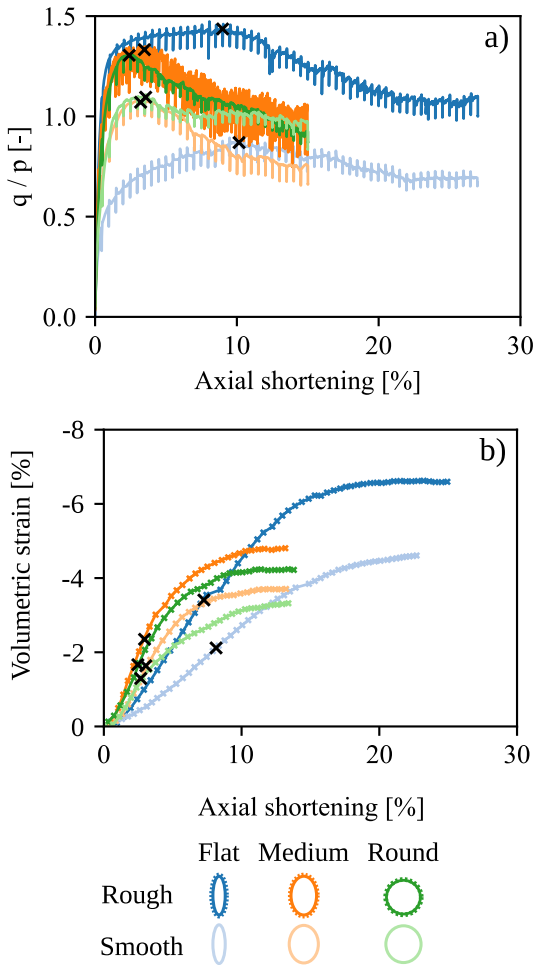


Figure 2. Macroscopic response of the specimens. a) Stress ratio (q/p) and (b) volumetric strain as a function of the axial shortening of the specimens. The occurrence of the peak stress ratio is marked with a cross symbol. The increased variability observed in the medium-rough specimen is due to a stick-slip interaction between the base plate and the piston, rather than the material response. An additional experiment with a different base plate confirmed a similar macroscopic response without stick-slip behavior.

These plots show an increase of the stress ratio up to a peak value $(q/p)_{peak}$, which is followed by a decrease toward a steady-state value by the end of the test, as typical in dense granular assemblies. It is important to note that regardless of the morphological features of the constituent particles, all specimens show the same overall evolution of q/p . Additionally, the greater variability observed in the medium-rough specimen is due to a stick-slip interaction between the base plate of the experimental setup and the piston, rather than the material's actual response. To confirm this, an additional triaxial compression experiment is conducted outside the X-ray tomography cabin using a different base plate, showing a similar macroscopic response without the stick-slip behavior.

One of the noticeable differences in terms of deformability of the specimens, is the maximum axial shortening attained. It is important to recall that the tests are stopped as soon as the base, which is allowed to slide laterally, contacts the inner wall of the triaxial cell. Specimens with flat particles achieve a maximum axial shortening of 30%, while the other specimens are stopped at 15%. As all specimens show a pronounced single strain localisation region, whose uniqueness is promoted by the sliding system, the variation in the maximum axial shortening already suggests some differences in the inclination of this band.

All specimens show a dilatant response since the beginning, which is typical of dense granular packings. Irrespective of the particle morphology, ε_v steadily rises and stabilises at a constant value at the end of the test. As observed in previous studies [Lin and Ng, 1997, Oda et al., 1985, Rothenburg and Bathurst, 1991, Salot et al., 2009, Ting et al., 1995], assemblies of elongated particles generally exhibit a larger final volumetric strain, which is typically attributed to the interlocking of the particles. This trend is also observed for the lower-friction assemblies, although this lower friction value leads to a reduction in the maximum achieved volumetric strain.

To further understand the dilatative behaviour of the specimens, Fig. 3 shows the evolution of the dilatancy angle Ψ computed as [Schanz and Vermeer, 1996]:

$$\sin(\Psi) = \frac{d\varepsilon_v/d\varepsilon_a}{d\varepsilon_v/d\varepsilon_a - 2} \quad (1)$$

where ε_a corresponds to the axial shortening. The dashed line shows the overall evolution of Ψ to better visualise the general behaviour. The dilatancy angle increases at the beginning of the test for all specimens, reaching a peak value (Ψ_{max}) occurring at the same axial strain as the peak stress ratio before decreasing towards 0° . Regardless of the inter-particle friction, the medium specimens exhibit the highest value of peak dilatancy. It might be expected that the assemblies of highly anisometric particles would show an even higher value of dilatancy, however, we observe that the rounded specimens have higher Ψ_{max} than the flat ones for both friction scenarios. This result, emerging solely from the morphology of the particles, suggests some fundamental differences in the underlying deformation mechanism at the particle scale.

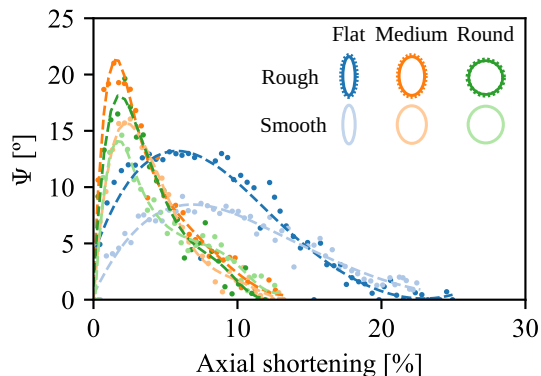


Figure 3. Dilatancy angle (Ψ) as a function of the axial shortening of the specimens

The relative motion between particles can in fact occur through two distinct mechanisms: *i*) rotation, or *ii*) relative sliding. If it is assumed that particle rotation is the dominant mechanism, then it could be expected that assemblies with particles of larger aspect ratio would exhibit a greater increase in ε_V and Ψ_{max} , compared to those with particles of lower aspect ratio. However, the results shown in Fig. 2 and Fig. 3 and do not entirely align with this assumption.

Alternatively, let us assume that particle sliding is the dominant mechanism. Considering that the anisometric shape of the particles favours an initial alignment of the small axis of the particles with the direction of gravity, then the relative height that a given particle must overcome to surpass another is higher for rounded particles (small axis of 3.2 mm) than for the medium or flat particles (small axis of 3.0 mm and 2.2 mm, respectively). This implies that the increase in volumetric strain and dilatancy should be more pronounced for specimens with rounded particles. This also partially contradicting the observed results.

These considerations suggest that the dominant deformation mechanism varies from one specimen to another, and thus, may be linked to the shape of the particles. Given their anisometry, it is conceivable that particle rotation is dominant for rounded particles, whereas particle sliding governs the deformation process in assemblies of flat particles. The abundance of both mechanisms can be quantified, as discussed in detail in the following sections.

3.2. Strain localisation

As mentioned previously, the displacement of the particles is projected onto a regular 3D grid, and a strain tensor is then computed for each cubic element. Although the volumetric (ε_V) and deviatoric (ε_q) strain fields are computed for all the strain increments along the test, only four increments, representative of 4 different phases of the response, are shown here for simplicity. Fig. 4(a) shows a sketch of the macroscopic stress-strain response observed for the specimens and the corresponding increments. Increment A is selected in the pre-peak regime, *i.e.*, strain-hardening phase and the build-up towards the peak stress (increment B). Increment C is selected in the post-peak regime, during the strain softening phase, while increment D is selected during the steady state observed at the end of the test. In all cases,

the strain increment corresponds to 0.5% axial shortening, *i.e.*, two consecutive scans.

As shown later, all the specimens present a well-defined shear band at the end of the test. To simplify the visualisation of the deformation processes, the shear band region is isolated at the end of the test using a threshold of $\varepsilon_q > 1\%$, and a Singular Value Decomposition (SVD) is performed over the region to obtain a local new orthogonal coordinate system. Fig. 4(b) shows the coordinate axis aligned with the shear band, where z' is the vector the vector normal to the shear plane, x' , is aligned with its inclination and y' , which is perpendicular to the other two vectors. The orientation of the vertical slices shown hereafter is in the plane $x' - z'$, *i.e.*, perpendicular to the orientation of the shear band of each test.

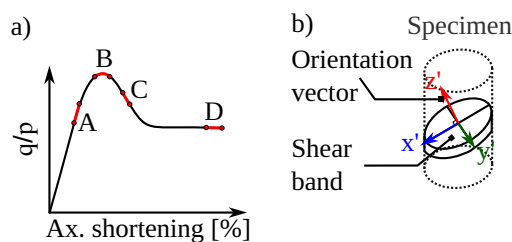


Figure 4. Strain localisation conventions. a) Selection of strain increments, b) Local coordinate system of the shear band

Figure 5 shows a comparative analysis of the incremental deviatoric and volumetric strain fields exhibited by the Flat-Rough and Medium-Rough specimens across the selected increments.

The pre-peak phase for the flat specimen manifests a diffuse pattern characterised by higher values of ε_q in its central region. Multiple deformation mechanisms are equally active at this point of the test, and no dominant direction is observed. Regions featuring high deviatoric strain also exhibit (positive) volume increases ($\varepsilon_V < 0$), consistently with the macroscopic dilative response observed previously. The sample made of medium particles, shows instead a strong concentration of ε_q in the lower half section in the pre-peak regime. It shows higher deviatoric strain than the flat specimen, already concentrated along a well defined direction. Additionally, the spatial distribution of the volumetric strain is wider and shows higher values compared to the flat specimen, as expected due to the greater amount of macroscopic dilation.

At increment B, corresponding to the peak stress ratio, the flat specimen exhibits a distinct strain localisation pattern, manifesting an inclination around 45° . Higher values of ε_q than at increment A are evident, pointing to an increase in concentration and magnitude of deviatoric strain along the emerging shear band. The incremental volumetric strain field shows higher dilation in this same region. In contrast, the medium specimen displays an even higher concentration of ε_q . Some local compaction events can already be observed inside the emerging shear band, pointing to some local rearrangement of particles.

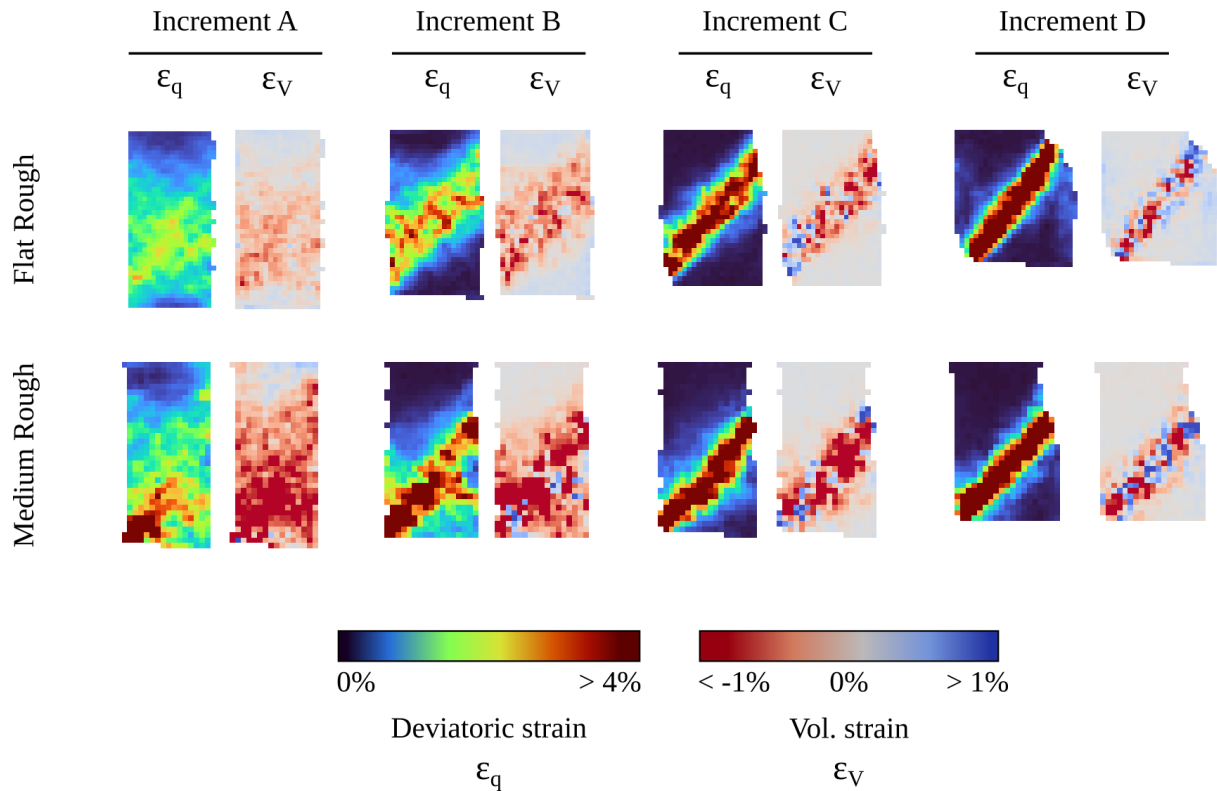


Figure 5. Incremental deviatoric and volumetric strain fields for selected instants of the flat-rough and medium-rough specimens

At increment C the specimens are beyond $(q/p)_{\text{peak}}$, and the stress ratio progressively diminishes towards a steady value. During this shear softening phase, both specimens exhibit a distinct shear band, within which elevated values of ε_q are observed, accompanied by a wide transition of deviatoric strain towards the non-deforming region ($\varepsilon_q \approx 0$). In contrast, the incremental volumetric strain fields show a decrease in the abundance of dilative regions and an increase of compactive events within the shear band. This observation suggests that within the shear band, localised particle rearrangement takes place, involving sliding or rotational events, which will be studied in the next section. Outside the shear band, the strain approaches negligible levels. As the specimens reaches a constant value of q/p (increment D), the incremental deviatoric strain field show a well consolidated shear band, with ε_q higher than 4%, and a sharp transition to the outside region. Within the shear band dilative and contractive events appear equally likely, suggesting an overall stable volumetric strain.

Although the previous figure only presents the evolution of two specimens, it portrays the overall evolution of the strain fields for the specimens test in this work. Slight differences are observed among the specimens. A complete discussion on their evolution, and the morphology of the final shear band is found in Pinzón [2023].

3.3. Particle kinematics

These sample-scale strain patterns are a consequence of particle rearrangements. Figure 6 shows vertical slices of the

sample, in which each grain is reported with a colour matching the magnitude of the rotation of the corresponding particle ($\|\omega\|$) for the increments B (peak stress ratio) and D (last strain increment) of all 12 specimens. The flat particle specimens already undergo high particle rotation in increment B, which concentrates in an area matching the strain localisation, while outside particles show $\|\omega\| \approx 0^\circ$. As these specimens are further deformed, $\|\omega\|$ further concentrates inside the strain localisation region. No clear effect of friction can be seen from these particle rotation fields.

The medium rough specimen shows a concentration of particle rotation in increment B, correlating to the emerging shear band, whereas the rotations in the medium smooth specimen are more homogeneous. At the steady state, both specimens show a clear concentration of $\|\omega\|$ along the shear band. This region is nevertheless much broader in the smooth specimen than in the rough one.

Finally, in rounded particle specimens the rotations evolve quite differently than the previous test: while some particles exhibit high rotation, no structured spatial distribution is apparent. This is despite the occurrence of a shear band with high ε_q . At the steady state, the particles inside the shear band appear to have a higher than average $\|\omega\|$, although the rotation is rather diffused. This can be explained by the fact that for nearly spherical particles, a local rotation does not necessarily affect the nearby particles, thus reducing the kinematic constraints of particle rotation. Conversely, for more elongated particles, the rotation is frustrated by the surrounding particles, since even small degrees of $\|\omega\|$ affect the surrounding ones.

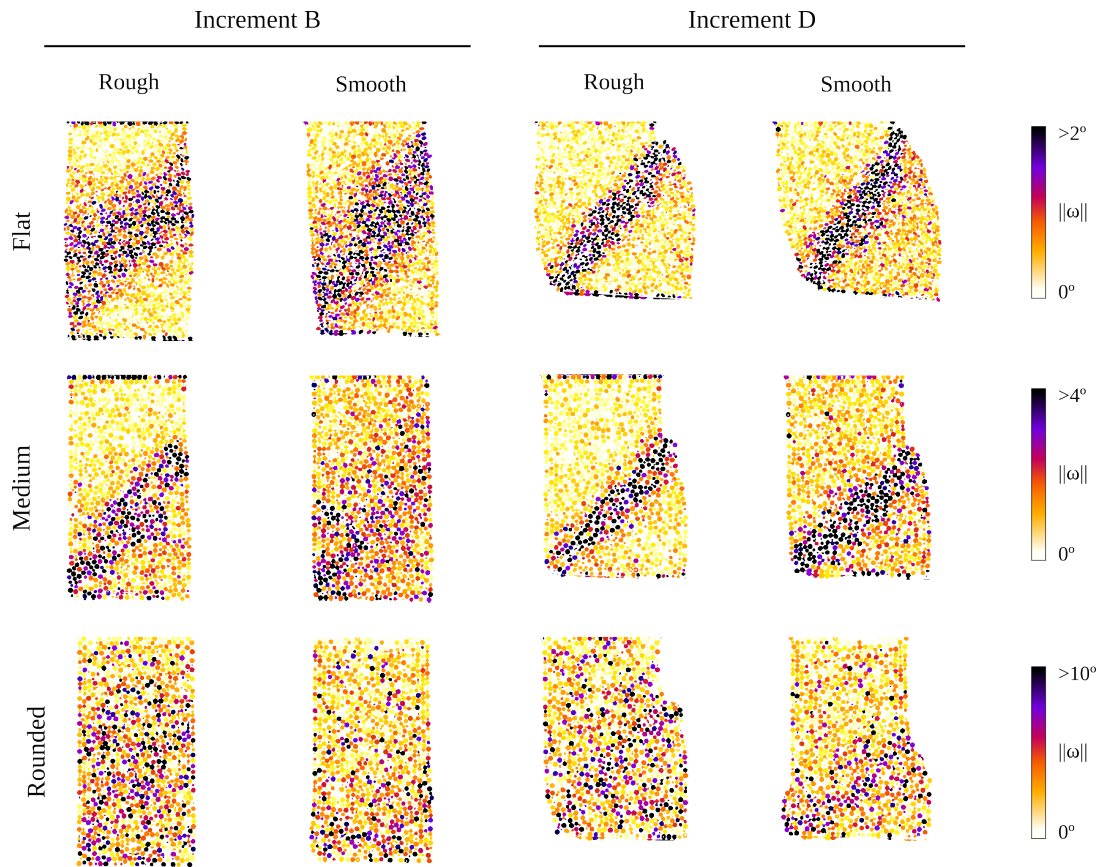


Figure 6. Particle rotation fields for increments B (peak stress) and D (steady state)

In general there is a noticeable difference between the rotation inside and outside the shear bands. To further understand this difference, we divide the particle in those within and outside the shear bands, as defined by the shear strain values. Figure 7(a) shows the evolution of the mean particle rotation ($\|\bar{\omega}\|$) inside and outside the shear bands as a function of the axial shortening of the specimens. To help identify the different phases of the test, the occurrence of the peak stress ratio is marked with a cross symbol.

It can be seen that for the flat specimens, particles in both subsets start to rotate during the strain-hardening phase, but more pronounced rotation takes place inside the emerging band. From 5% of axial shortening onwards, rotation continues to increase inside the band, while decreasing outside it. Friction appears to have marginal effect within as well as outside the band.

For the medium specimens, a strong increase of rotations inside the shear band can be observed up to the peak stress ratio, while outside of it, the value of $\|\bar{\omega}\|$ continuously decreases. At 7% of axial shortening the mean rotation stabilises across the sample. It is important to note that inter-particle friction plays a stronger role for these specimens than for their flat counterpart, increasing rotation when decreasing friction. Additionally, the magnitude of mean particle rotation is almost twice that of the flat specimens, likely due to the lower degree of particle interlocking. Finally, for the rounded specimens, the mean particle rotation increases during the strain hardening phase within the

band while decreasing outside. In both cases, a steady value is attained around 5% of axial shortening, and is considerably higher than for the previous specimens. In this case higher friction induces higher rotation.

For all cases, the end of the test is marked by a shear band where particle rotation is highly concentrated and stable in value. To further explore the differences induced by the particle shape and inter-particle friction at this state, Fig. 7(b) reports the probability density function of the particle rotation values within the shear band for the last strain increments of all tests. Given the fluctuations in the number of particles contained in each specimen, the histograms are normalised so that the integral over the angle range is always equal to 1. It is clear that there is a strong effect of the aspect ratio on the distribution of rotation values among the particles. Both the average and the standard deviation increase with the sphericity of the particles and their smoothness (except, this latter, for the round particles). This supports the previous observations on the importance of interlocking on particle rotation. Highly anisometric particles have to rotate coherently with their neighbours because of the high level of interlocking, while for more rounded particles, local events of high rotation can take place without strongly affecting their surroundings.

Another key kinematic feature of the particles, complementary to their rotation, is their incremental displacement. Notably the direction of displacement is of great interest to understand the development of preferential directions.

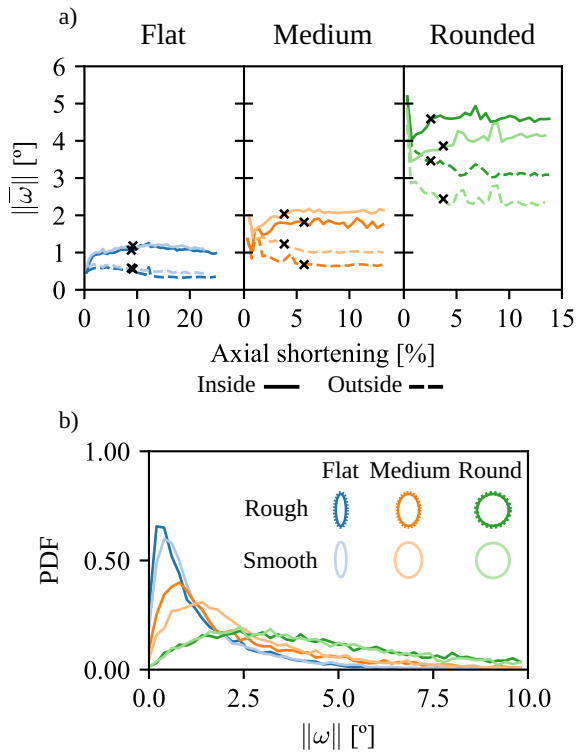


Figure 7. Particle rotation within the shear band. a) Mean particle rotation inside (continuous line) and outside (dashed line) of the shear band region, b) Probability density function of particle rotation within the shear band for the last strain increment.

Considering the strong connection between strain localisation and particle kinematics, the incremental displacement vectors are projected onto a characteristic axis of the shear band. Using the coordinate system of the strain localisation region shown in Fig. 4(b), each vector is projected onto the x' axis, *i.e.*, the direction of maximum inclination of the shear band.

Figure 8 shows vertical slices of the projected incremental displacement ($\|d_{x'}\|$) for the increments B and D of all specimens. It should be reminded that the load is applied (upwards) at the bottom of the specimen. As the stress ratio reaches its peak at increment B, the incremental displacement along the shear band direction increases. Because of the well-defined shear band, the displacement field can be described using a simple kinematic model of two blocks sliding along a plane. For all the specimens, a noticeable transition zone appears between the lower block, registering displacements around 7 pixels, and the, essentially static, upper block. At this stage, a sharp gradient is evident in the flat specimens, as well as in the medium-rough, whereas a more diffuse transition zone is observed for the other specimens.

By increment D, the transition zone narrows, containing only a few grains (3-4 particles), as the shear band reaches its final morphology. For all specimens, except the flat-smooth, the incremental displacements within the lower block remain relatively uniform at 7 pixels. As expected, the steady

state is characterised by a concentration of incremental displacements along the shear band direction, distinctly separating the two kinematic blocks. A slight horizontal gradient is observed for the lower block of the flat-smooth specimen, suggesting a minor rotation of the bottom end.

Figure 9 illustrates the probability density function of the incremental displacement (δd) inside the shear band at the end of the test. It reveals two prominent peaks: the first, around 1 pixels, and the second around seven to nine pixels. This bimodal distribution of δd suggests that the chosen area encompasses both the band and part of the surrounding area (including particles from the upper static block as well as the lower one).

As expected, the first peak remains stable across all specimens, while the second peak is a function of particle shape and friction. Flat particles might be expected to exhibit a greater magnitude of incremental displacement, as their shape facilitates particle sliding along the long axis. Similarly, smooth particles, could be expected to display a higher δd . Surprisingly, the distributions reveal a different response.

The medium-rough specimen exhibits the highest particle incremental displacement, followed by the flat-rough and rounded-rough, while the flat-smooth specimen displays the lowest value of δd . These variations can be attributed to the interlocking degree associated with a specific particle shape. In the case of flat particles, sliding is enhanced by particle alignment; otherwise, their aspect ratio induces rotation over sliding. Within the shear band, the deformation process forces particle rotation. Despite the flat-rough specimen having the highest initial particle alignment, as can be observed from Table 1, the incremental displacement magnitude is significantly limited by interlocking. Conversely, the elevated δd value of the medium-rough specimen suggests that its intermediate aspect ratio promotes particle sliding along the long axis, accompanied by reduced interlocking.

Nevertheless, the previous interpretation fails to justify the role of friction, which appears to always favour displacement. To understand this counter-intuitive result, it helps to remember the initial particle alignment in the specimens in Table 1. Assemblies with lower friction exhibit in fact a more isotropic initial arrangement, which limits their interlocking, which emerges from the more disorganised assemblies of high-friction scenarios. The initial anisotropy is a successful predictor in fact of both the role of friction and the response of flat-smooth specimen, which displays the lowest value of δd . Not only this specimen shows a substantially lower value of initial particle arrangement, but also the higher aspect ratio of the flat particles strongly obstructs particle sliding. It is important to note that in the previous analysis, the movement of the centre of mass of the particles is a consequence of both sliding and rotation.

4. Discussion

Since failure is accommodated by the emergence of a shear band in all specimens, distinguishing particle kinematics within it, and relating it to the bulk response is therefore

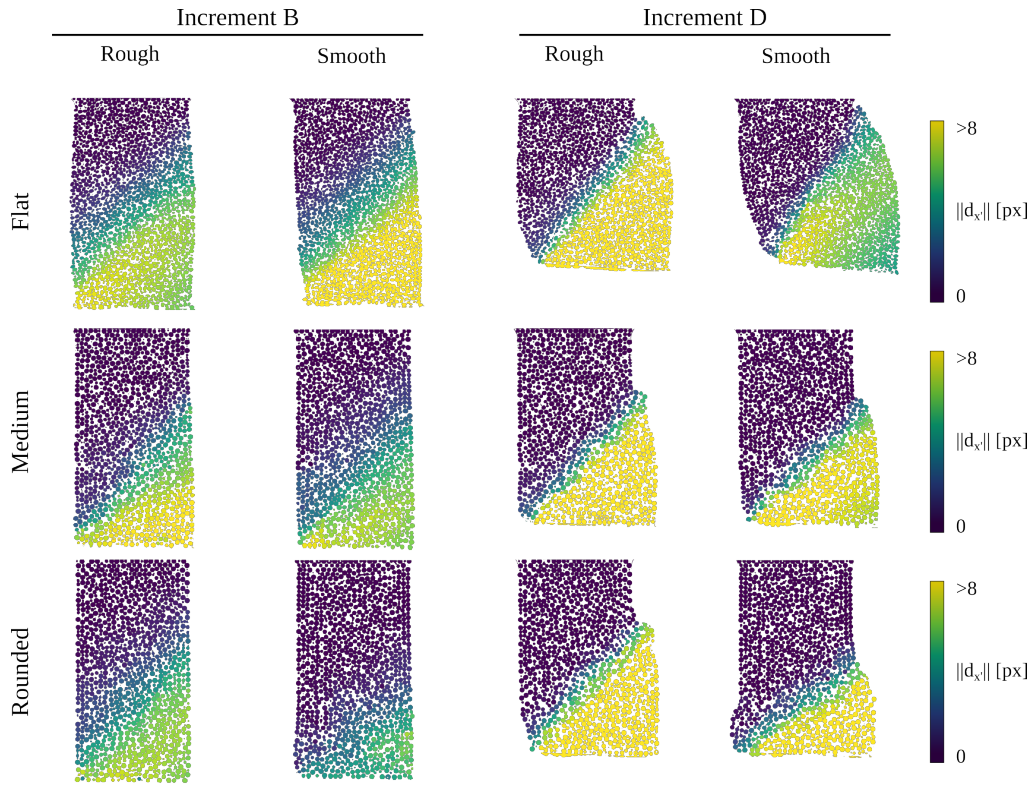


Figure 8. Particle incremental displacement along the shear band direction for increments B (peak stress) and D (steady state)

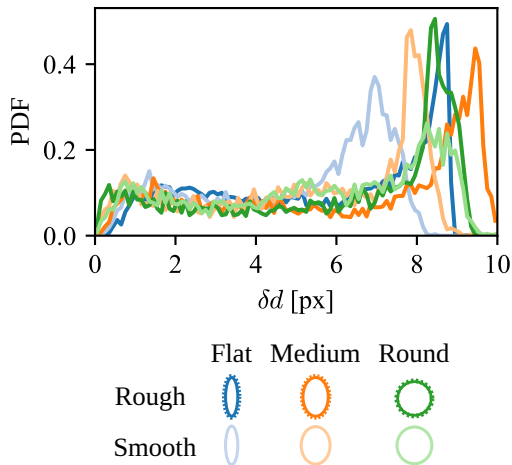


Figure 9. Probability density function of the incremental displacement magnitude (δd) for particles within the shear band at increment D.

crucial. Figure 10(a) shows the mean incremental deviatoric strain ($\bar{\epsilon}_q$) inside the shear band throughout all test. Like before, the occurrence of the peak stress ratio is marked by a cross. Flat particles, exhibit a rapid increase in $\bar{\epsilon}_q$, and followed by a more gradual increase ultimately approaching a plateau around the end of the test. Specimens characterized by medium and rounded particles exhibit instead a consistent increase during the strain hardening phase followed by a plateau starting around their peak stress ratio.

It appears that the mean incremental deviatoric strain is unaffected by the inter-particle friction value and converges to a comparable value across all tests, around 3% by the end of the test. This may suggest that the degree of distortion within the shear band is independent of both particle shape and inter-particle friction.

The evolution of $\bar{\epsilon}_q$ appears to exhibit a pattern similar to that of the incremental particle rotation within the shear band, previously illustrated in Fig. 7(a). To visualise the correlation between these two variables, Fig. 10(b) shows the evolution of average incremental deviatoric strain as a function of the average incremental rotation for particles within the shear band. The start of the test is marked by a circle, while its end is denoted by a triangle. A linear relationship between these variables is evident for all scenarios, highlighted by the grey band in the plots. After the initial point, the evolution of these two variables within the shear band is remarkably coherent. This might suggest that particle rotation plays a dominant role contributing to deviatoric strain within the specimens, which principally develops during the strain hardening phase.

Figure 11(a) focuses on the other main strain component: the mean incremental volumetric strain ($\bar{\epsilon}_v$), again selecting the grains that make up the shear band. As expected, the specimens predominantly exhibit dilative behaviour, in agreement with the macroscopic measurements derived from the bulk response (see Fig. 2 and Fig. 3).

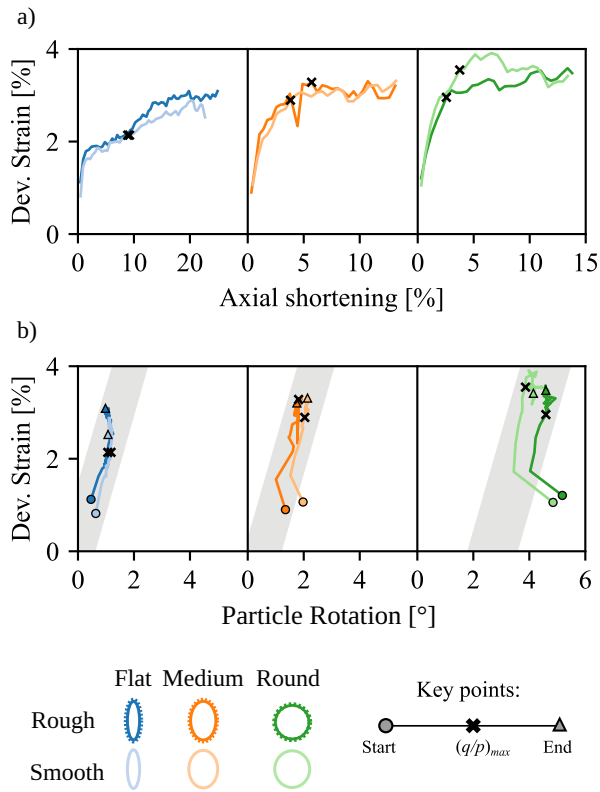


Figure 10. Incremental deviatoric strain as a function of axial shortening (a) and particle rotation (b) for the particles within the shear band.

All specimens show a rapid increase followed by a gradual decrease towards a stable volumetric strain. The peak occurs either at, or slightly after, the peak. For specimens composed of flat particles, this increment is more modest than in the other samples. Interparticle friction appears to induce smaller incremental volumetric strain, which is consistently lower in the strain-hardening phase than for rough particles. As shown in the incremental strain field in Fig. 5, the post-peak phase is characterised by the simultaneous occurrence of local dilative and contractive events within the shear band, which explains the convergence of the average incremental volumetric strain towards zero.

The ability to measure a local strain tensor, based on particle displacements, enables the exploration of the effects of particle morphology on the onset of critical state, *i.e.*, a continuous shear deformation with a constant volume under constant stress. Macroscopically, the results of Fig. 2(a) show that the stress ratio reaches, or starts reaching, a constant value at the end of the test, thus fulfilling the stress condition. Similarly, the macroscopic volume attains a constant value at the end of the test as seen in Fig. 2(b), which suggests that the strain condition of the critical state framework is also fulfilled. Inside the strain localisation region, the local measurements of volumetric strain in Fig. 11(a) reveal that the volume inside the shear band is reaching a constant value as well. However, it is impossible to retrieve the local value of stress from the experimental data, and thus, a complete assessment of the onset of critical state inside the shear band can not be performed.

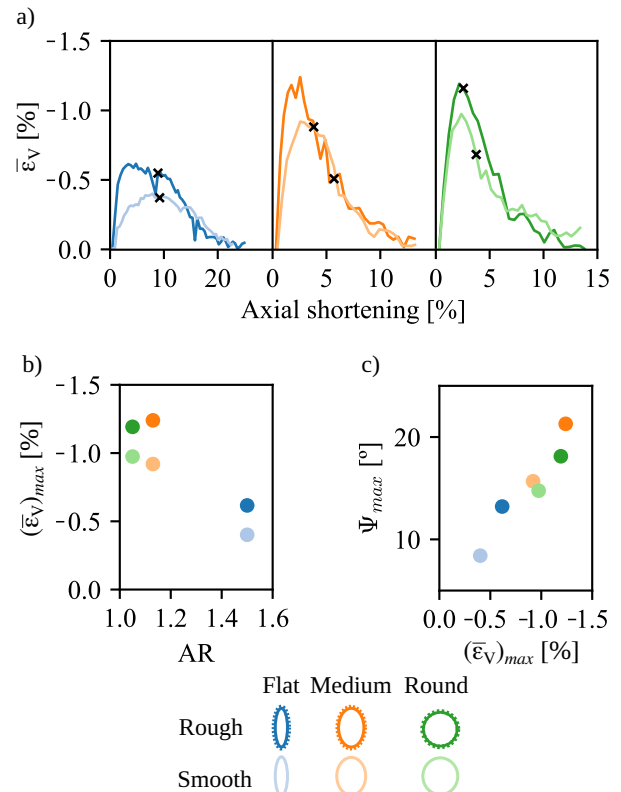


Figure 11. Evolution of incremental volumetric strain. (a) Evolution as a function of axial shortening, (b) Relation between the maximum incremental volumetric strain and the aspect ratio of the particles, and (c) Relation between the maximum dilatancy and the maximum incremental volumetric strain for the particles within the shear band.

It is important to note that, the apparent local convergence towards a critical state is only achieved after a considerable amount of local shear, varying between 50% and 80% for the rounded and flat particles, respectively. This difference can be linked to the competition between the different deformation mechanisms exposed earlier (*i.e.*, particle rotation versus particle sliding).

Finally, the relationship between the maximum dilative incremental strain ($(\bar{\epsilon}_V)_{max}$) and the particle shape is shown in Fig. 11(b). A correlation can be observed between these variables, with flat particles exhibiting lower maximum dilatancy than the rest, and smoother particles being consistently less dilatant than their rougher counterpart. The former can be explained as a result of the magnitude of particle rotation, which is constrained for elongated particles.

The Medium-Rough specimen displays is the main anomaly in this otherwise linear correlation, showing a slightly higher value of $(\bar{\epsilon}_V)_{max}$ than the Rounded-Rough specimen, mirroring the bulk measurements of bulk dilatancy (Ψ_{max}) presented earlier in Fig. 3. These variables are shown together in Fig. 11(c), revealing a clear positive correlation between them. While the incremental values of ϵ_V contribute to the computation of Ψ , as outlined in Eq. 1, it is important to note that these variables are measured

using different techniques and represent different domains. While the former corresponds to a bulk assessment and is measured from the position of the particles, the latter is the volumetric change inside the shear band and is determined based on the measured grain kinematics.

It can be observed that higher values of $(\bar{\epsilon}_V)_{max}$ correlate with higher values of Ψ_{max} . However, the Medium-Rough specimen exhibits substantially higher peak dilatation than the Rounded-Rough specimen, despite a relatively minor difference in maximum dilative incremental strain. This implies that particle rotation alone cannot account for the development of volumetric strain and, ultimately, bulk peak dilatancy. Notably, rounded particles exhibit considerably higher values of rotation than medium particles. Instead, a combination of interlocking and particle rotation contributes to higher values of volumetric strain. For the case of the specimens with rounded particles, their spherical shape enhances the rotation of individual particles but limits their interaction with their neighbour, as evidenced by their diffuse rotation fields shown previously.

In contrast, the larger aspect ratio of the flat particles implies that the rotation of any given particle would have a greater impact the displacement of the surroundings particles. This strong interlocking clearly also limits the rotation and limits the dilation of the specimens. Conversely, the Medium-Rough particles show a higher particle rotation than the Flat-Rough, but a higher interlocking than Rounded-Rough, resulting in higher values of peak dilatancy.

5. Conclusion

This study explores the effects of inter-particle friction and particle shape on the deformation processes of granular materials. By using ellipsoidal particles with three aspect ratios and two interparticle friction coefficients, six monodisperse specimens are tested in triaxial compression while being imaged using x-ray tomography *in-operando*. A scan is performed each 0.5 % of axial shortening, resulting in more than 30 scans per test. Each of the particles of the specimens is identified and tracked for each the strain increments. The measured displacement field of the particles is projected onto a regular grid and used to compute strain fields, allowing the study of the evolving local deformation processes. The measured displacement and rotations of the individual particles are also used to evaluate the local kinematics and their relations to the macroscopic strain.

A consistent dilative response is evident since the initial stages of all tested specimens, reaching a constant value at the end of the test. At the macroscopic scale, an increase in the aspect ratio of particles induces higher total volumetric strain.

The incremental strain fields highlight how strain hardening corresponds to pronounced dilation, accompanied by the emergence of a shear band for all specimens. Beyond the peak stress ratio, strain localisation becomes predominant and volumetric strain stabilises, with local compressive and dilative events counterbalancing within the shear band. The strain localisation region is found to correspond

to higher particle rotations, with magnitudes strongly varying depending on the samples. Specimens with flat particles exhibit a concentration of the rotation of grains in a narrower band, as well as a lower average particle rotation of only 2° . Rounded particles display a more diffuse spatial distribution as well as higher particle rotation, reaching up to 10° .

The study of the particle displacement field reveals the emergence a two-block system, divided by the shear band and sliding on top of each other. Contrary to expectations, the specimens that show the greatest amount of particles displacement are not those with flat particles, but rather those with medium rough particles. This is ascribed to the stronger interlocking among flat particles, as local deviations from a perfectly aligned particle arrangement force the particles to rotate to move.

In essence we observe the important role played by particle interlocking at all scales, which is influenced by particle anisometry. Rounded particles promote rotation due to lower interlocking, but this diminishes the impact of local kinematic events on direct neighbours. Flat particles, exhibit strong interlocking, enhancing the influence that rotation events have on their surroundings. However, this interlocking also constrains particle rotation, limiting their occurrence. It is found that the medium rough particles have the right combination of high interlocking and moderate restriction to particle rotation, which generated the most pronounced dilatancy of all specimens tested in this work.

It is important to highlight that the use of well-controlled monodisperse assemblies adopted in this work, isolates and accentuates the effects that arise from the morphology of the particles. The micro-mechanical observations presented in this work cannot nevertheless be directly generalised to all granular materials due to the shape polydispersity typical in natural materials, which may attenuate the effects reported here. Nonetheless, it can be expected that the micro-mechanical effects detailed in this work govern the interactions at the particle scale.

Conflicts of Interest

The authors declare that there is no conflict of interest. The complete review history is available online.

Data availability

All the data sets generated during this study are available in an open repository and can be obtained here: <https://doi.org/10.5281/zenodo.8014905>.

Acknowledgements

The authors thank Prof. Matthew Coop for advice on experimental design of the inter-particle shearing device.

This project has received funding from the European Union's Horizon 2020 research and innovation program under the Marie Skłodowska-Curie grant agreement No. 812638 (CALIPER). Laboratoire 3SR is part of the LabEx Tec 21 (Investissements d'Avenir - grant agreement n°ANR-11-LABX-0030)

References

- Abbireddy, C. and Clayton, C. (2015). The impact of particle form on the packing and shear behaviour of some granular materials: an experimental study. *Granular Matter*, 17:427–438.
- Alsaleh, M. I., Alshibli, K. A., and Voyiadjis, G. Z. (2006). Influence of micromaterial heterogeneity on strain localization in granular materials. *International Journal of Geomechanics*, 6(4):248–259.
- Alshibli, K. A. and Alsaleh, M. I. (2004). Characterizing surface roughness and shape of sands using digital microscopy. *Journal of computing in civil engineering*, 18(1):36–45.
- Andò, E., Dijkstra, J., Roubin, E., Dano, C., and Boller, E. (2019). A peek into the origin of creep in sand. *Granular matter*, 21:1–8.
- Andò, E. and Viggiani, G. (2018). On the ease of experimental access to deformation entities in granular assemblies. *Ital. Geotech. J.*, 52(2):44–51.
- Andò, E., Viggiani, G., Hall, S. A., and Desrues, J. (2013). Experimental micro-mechanics of granular media studied by X-ray tomography: recent results and challenges. *Géotechnique Letters*, 3(3):142–146.
- Antony, S. and Kruyt, N. (2009). Role of interparticle friction and particle-scale elasticity in the shear-strength mechanism of three-dimensional granular media. *Physical Review E*, 79(3).
- Azéma, E., Estrada, N., and Radjai, F. (2012). Nonlinear effects of particle shape angularity in sheared granular media. *Physical Review E*, 86(4).
- Azéma, E. and Radjai, F. (2010). Stress-strain behavior and geometrical properties of packings of elongated particles. *Physical Review E*, 81(5).
- Azéma, E., Radjai, F., and Dubois, F. (2013). Packings of irregular polyhedral particles: Strength, structure, and effects of angularity. *Physical Review E*, 87(6).
- Azéma, E., Radjai, F., Peyroux, R., and Saussine, G. (2007). Force transmission in a packing of pentagonal particles. *Physical Review E*, 76(1).
- Bagi, K. (1996). Stress and strain in granular assemblies. *Mech. Mater.*, 22(3):165–177.
- Barreto, D. and O’Sullivan, C. (2012). The influence of interparticle friction and the intermediate stress ratio on soil response under generalised stress conditions. *Granular Matter*, 14:505–521.
- Binaree, T., Azéma, E., Estrada, N., Renouf, M., and Preechawuttipong, I. (2020). Combined effects of contact friction and particle shape on strength properties and microstructure of sheared granular media. *Physical Review E*, 102(2).
- Casas, N., Mollon, G., and Daouadji, A. (2022). Dem analyses of cemented granular fault gouges at the onset of seismic sliding: peak strength, development of shear zones and kinematics. *Pure and Applied Geophysics*, 179(2):679–707.
- Cavarretta, I., Rocchi, I., and Coop, M. R. (2011). A new interparticle friction apparatus for granular materials. *Canadian Geotechnical Journal*, 48(12):1829–1840.
- Desrues, J. and Viggiani, G. (2004). Strain localization in sand: an overview of the experimental results obtained in Grenoble using stereophotogrammetry. *Int. J. Numer. Anal. Methods Geomech.*, 28(4):279–321.
- Estrada, N., Azéma, E., Radjai, F., and Taboada, A. (2011). Identification of rolling resistance as a shape parameter in sheared granular media. *Physical Review E*, 84(1).
- Hall, S. A., Bornert, M., Desrues, J., Pannier, Y., Lenoir, N., Viggiani, G., and Bésuelle, P. (2010). Discrete and continuum analysis of localised deformation in sand using X-ray μ CT and volumetric digital image correlation. *Géotechnique*, 60(5):315–322.
- Katainen, J., Paajanen, M., Ahtola, E., Pore, V., and Lahtinen, J. (2006). Adhesion as an interplay between particle size and surface roughness. *Journal of colloid and interface science*, 304(2):524–529.
- Kong, D. and Fonseca, J. (2019). On the kinematics of shelly carbonate sand using X-ray micro tomography. *Engineering Geology*, 261.
- Krumbein, W. C. (1941). Measurement and geological significance of shape and roundness of sedimentary particles. *Journal of Sedimentary Research*, 11(2):64–72.
- Lin, X. and Ng, T.-T. (1997). A three-dimensional discrete element model using arrays of ellipsoids. *Geotechnique*, 47(2):319–329.
- Mirghasemi, A., Rothenburg, L., and Matyas, E. (2002). Influence of particle shape on engineering properties of assemblies of two-dimensional polygon-shaped particles. *Geotechnique*, 52(3):209–217.
- Miura, K., Maeda, K., Furukawa, M., and Toki, S. (1998). Mechanical characteristics of sands with different primary properties. *Soils and foundations*, 38(4):159–172.
- Nadler, B., Guillard, F., and Einav, I. (2018). Kinematic model of transient shape-induced anisotropy in dense granular flow. *Physical review letters*, 120(19).
- Oda, M., Konishi, J., and Nemat-Nasser, S. (1982). Experimental micromechanical evaluation of strength of granular materials: effects of particle rolling. *Mechanics of materials*, 1(4):269–283.
- Oda, M., Nemat-Nasser, S., and Konishi, J. (1985). Stress-induced anisotropy in granular masses. *Soils and foundations*, 25(3):85–97.
- Oda, M., Takemura, T., and Takahashi, M. (2004). Microstructure in shear band observed by microfocus X-ray computed tomography. *Géotechnique*, 54(8):539–542.
- Pena, A., Garcia-Rojo, R., and Herrmann, H. J. (2007). Influence of particle shape on sheared dense granular media. *Granular matter*, 9(3-4):279–291.
- Pinzón, G. (2023). *Experimental investigation of the effects of particle shape and friction on the mechanics of granular media*. PhD thesis, Université Grenoble Alpes.
- Pinzón, G., Andò, E., Tengattini, A., and Viggiani, G. (2023). Experimental investigation of the effects of particle shape and friction on the mechanics of granular media. Zenodo dataset available at <https://doi.org/10.5281/zenodo.8014905>.
- Rorato, R., Arroyo, M., Gens, A., Andò, E., and Viggiani, G. (2021). Image-based calibration of rolling resistance in

- discrete element models of sand. *Computers and Geotechnics*, 131.
- Rothenburg, L. and Bathurst, R. (1992). Micromechanical features of granular assemblies with planar elliptical particles. *Geotechnique*, 42(1):79–95.
- Rothenburg, L. and Bathurst, R. J. (1991). Numerical simulation of idealized granular assemblies with plane elliptical particles. *Computers and geotechnics*, 11(4):315–329.
- Rousé, P., Fannin, R., and Shuttle, D. (2008). Influence of roundness on the void ratio and strength of uniform sand. *Géotechnique*, 58(3):227–231.
- Saint-Cyr, B., Delenne, J.-Y., Voivret, C., Radjai, F., and Sornay, P. (2011). Rheology of granular materials composed of nonconvex particles. *Physical Review E*, 84(4).
- Salot, C., Gotteland, P., and Villard, P. (2009). Influence of relative density on granular materials behavior: Dem simulations of triaxial tests. *Granular matter*, 11(4):221–236.
- Santamarina, J. C. and Cho, G.-C. (2004). Soil behaviour: The role of particle shape. In *Advances in geotechnical engineering: The Skempton conference*, pages 604–617. Thomas Telford Publishing.
- Schanz, T. and Vermeer, P. (1996). Angles of friction and dilatancy of sand. *Géotechnique*, 46(1):145–151.
- Senetakis, K. and Coop, M. (2014). The development of a new micro-mechanical inter-particle loading apparatus. *Geotechnical Testing Journal*, 37(6):1028–1039.
- Shahin, G. and Hurley, R. (2022). Hp-TACO: A high-pressure triaxial compression apparatus for in situ x-ray measurements in geomaterials. *Review of Scientific Instruments*, 93(11).
- Stamati, O., Andò, E., Roubin, E., Cailletaud, R., Wiebicke, M., Pinzón, G., Couture, C., Hurley, R. C., Caulk, R., Cailletie, D., et al. (2020). Spam: software for practical analysis of materials. *Journal of Open Source Software*, 5(51).
- Taboada, A., Chang, K.-J., Radjai, F., and Bouchette, F. (2005). Rheology, force transmission, and shear instabilities in frictional granular media from biaxial numerical tests using the contact dynamics method. *Journal of Geophysical Research: Solid Earth*, 110(B9).
- Ting, J. M., Meachum, L., and Rowell, J. D. (1995). Effect of particle shape on the strength and deformation mechanisms of ellipse-shaped granular assemblages. *Engineering computations*, 12(2):99–108.
- Tudisco, E., Jailin, C., Mendoza, A., Tengattini, A., Andò, E., Hall, S. A., Viggiani, G., Hild, F., and Roux, S. (2017). An extension of digital volume correlation for multimodality image registration. *Measurement Science and Technology*, 28(9).
- Wadell, H. (1932). Volume, shape, and roundness of rock particles. *The Journal of Geology*, 40(5):443–451.
- Xiao, Y., Long, L., Matthew Evans, T., Zhou, H., Liu, H., and Stuedlein, A. W. (2019). Effect of particle shape on stress-dilatancy responses of medium-dense sands. *Journal of Geotechnical and Geoenvironmental Engineering*, 145(2).
- Yuan, Y., Jiao, Y., Wang, Y., and Li, S. (2021). Universality of jammed frictional packing. *Physical Review Research*, 3(3).
- Zhang, B. and Regueiro, R. A. (2015). On large deformation granular strain measures for generating stress–strain relations based upon three-dimensional discrete element simulations. *International Journal of Solids and Structures*, 66:151–170.
- Zhou, B., Huang, R., Wang, H., and Wang, J. (2013). Dem investigation of particle anti-rotation effects on the micromechanical response of granular materials. *Granular Matter*, 15:315–326.
- Zingg, T. (1935). *Beitrag zur schotteranalyse*. PhD thesis, ETH Zurich.

Manuscript received 27th October 2024, revised 13th February 2025, accepted 20th February 2025.